

River Flooding on Taipei City Area Inundation

Reui-Kuo Lin, Taipei College of Maritime Technology, Taiwan
Kwan Ouyang, Taipei College of Maritime Technology, Taiwan
Jen-Chieh Wu, Taipei College of Maritime Technology, Taiwan
Shi-Min Lee, Tamkang University, Taiwan

The Asian Conference on Sustainability, Energy and the Environment 2015
Official Conference Proceedings

Abstract

Owing to geographic location of Taiwan being on subtropical monsoon zone, so typhoons and storms occur frequently. Typhoons and storms during summer and fall always cause several flooding, flood damages, and human lives loss in Taiwan. The major factors that cause flooding, landslide, and debris-flow in Taiwan are typhoons and storms of monsoon rain season. The function of hydraulic structure has its limit, it must cooperate with urban flood improvement action to mitigate flood damages. The urban flood improvement action must improve the locations of flood area, flood depth, flood duration, and calculate flood damages in the floodplain when heavy rainfall happens and effectively mitigate the flood disaster loss.

We present a two-dimensional unsteady flow model based on the TVD finite difference method with structured grids in basin system. The Digital Terrain Model (DTM) is employed to treat the input and output data for the model. The final goal of this project is to simulate Taipei city (Shilin area) and provide the most important information, including the inundation range and depth for Shilin. As an important aid to the flood improvement action review and evaluation for warming policy, and prepare step of decision. Then, we test the suitability of this model on Taipei city (Shilin area), and present the result and discuss.

iafor

The International Academic Forum
www.iafor.org

Introduction

Flooding damaged river upstream reservoir numerical model of development, mainly to assess potential flooding floods in Taiwan. Simulation can be divided into a barrage of destruction, namely dam break flood; calculus of categories and flooding downstream. Dam-break flood simulation, thrust in a simulated dam collapse caused by the severity of the flood, flood extent and the degree of loss of life and property downstream areas could cause it to develop emergency contingency measures, to assess reservoir potential disaster to assist reservoir downstream catchment area development plans and the preparation of flood simulation.

Dam-break flow phenomena for the free surface of the problem contained, while the free surface in the method of calculating the movement of fluid interface, usually divided into Eulerian description and Lagrangian description. Euler's description on behalf of all computing grid is fixed in space, a fixed-point observation of fluid particle motion. The pull is observed moving description of the fluid particles, due to the fluid motion of the free surface will therefore flow field grid computing movement must follow immediately, namely mobile grid. This section provides a brief introduction to the free surface of the processing method, comprising: a marked grid method (MAC), the volume of fluid method (VOF), level set method (LSM). Also listed in recent years, many scholars and research results of the free surface.

Stay (1988) in order to deal with change, not the free surface boundary fixed by the coordinates conversion method, containing free surface boundary changes ilk field, into a fixed border area, and then be parsed to the finite element method. Solving the pressure field is concerned, the use of class Simple speed correction method. Finally, we discuss the circulation field containing the free surface of the fluid container and observe the two-dimensional turbulence freedom movement. Liao (1994) to the incompressible Navier-Stokes equations with the boundary coordinates adhesion method for solving free surface containing ilk field for much of the change in the free surface flow situations, such as fluctuations in the reservoir water problem, there's a good result.

Huang (1998) studied the phenomenon of droplet collision and fusion, the idea of using multi-fluid system (multi-fluid) of the surface of the droplets regarded system density discontinuity, the use of surface capturing method to automatically calculate

the position and shape of the droplet. The only effect of surface tension on the interface between different liquids, in theory, no thickness will cause computational difficulties, so this research to take continuous surface force model (continuum surface force, CSF), so that the free surface has a thickness, then the surface tension is expressed as of a continuous physical (body force) form, distributed in the volume percentage of the free surface.

Mark Sussman (2000) allelic combination function method and fluid volume method, developed couples level set/volume of fluid (CLSVOF), and calculate the free surface two-phase flow problems. Development of this algorithm design is to calculate the surface tension and the free surface, can produce a more accurate ratio of the volume of fluid method or methods allelic function method. This article discuss buoyant bubbles, the bubbles merge the two issues found in the treated surface tension than the volume of fluid method is good, because the surface is relatively simple to calculate, but also more accurate than the mass conservation issues such as potential function method. Euler equation viewpoint taken to a fixed grid space observed fluid changes. The free surface of the particle tracking method were used, the volume of fluid method. Finally, we discuss the shock wave of finite amplitude, transmission and reflection of solitary waves. Hung (2002) CIP (cubic interpolated profile) method to simulate the free surface and the flow field, focuses on the CIP method for different thickness of the free surface of the grid scenarios capture and study there, without affecting the flow field of the viscous force . In the case of water droplets falling to explore the ability to simulate the surface, the viscous force found that the shape of the free surface has its influence exists.

Guo (2002), the use of allelic function method for solving the two-dimensional free surface flows. And two-dimensional reservoir rippling problems dimensional dam-break flow field, the freedom to do validation or water and other cases. Numerical results for the initial discovery of the border merger, crushing the capture quite good results. Lu (2003) also allelic function method free surface of a two-dimensional flow problems. Also adding to verify Zalesak problem allelic function method, the weight of the correctness of the distance, and then within the convective flow field after field solution of the ladder reliability verification flow numerical model. Finally, after the free surface to simulate the ladder, jump water issues and other cases, for the consolidation of the free surface, crushing the capture also have good results. Chen (2004), the use of allelic function method for solving the three-dimensional free surface flows of. Will be extended to three-dimensional problems. Allelic function equation solving section, space, and time entries were

used WENO France and third-order Runge-Kutta method to discrete. Finally, simulation examples include: dry bed dimensional dam-break issue, freedom or water and droplet collision.

The outline of this paper is as follows: In Section 2, the differential equations governing the motion of two fluids will be presented along with the transport equations for the fluid viscosity and density. In Section 3, the truly two-dimensional dispersion-relation-preserving advection scheme will be presented to dispersively more accurate advect the front of interface. Section 4 is addressed to investigate the dam-break, bubble rising, and Rayleigh-Taylor instability problems. Finally, we will draw some conclusions in Section 5.

Governing equations

Of the two immiscible fluids under current investigation, one is known as a liquid and the other is a gas. Both of them are considered to be incompressible. The resulting equations of motion for the gas and liquid fluids in a gravitational vector field g can be represented by the incompressible Navier-Stokes equations given below:

$$\frac{\partial \underline{u}}{\partial t} + (\underline{u} \cdot \nabla) \underline{u} = \frac{1}{\rho} (-\nabla p + \nabla \cdot (2 \underline{\underline{D}}) - \underline{\underline{T}} + \rho \underline{\underline{g}}) \quad (1)$$

$$\nabla \cdot \underline{\underline{u}} = 0 \quad (2)$$

where the physical properties ρ and μ shown in equation (1) represent the fluid density and the fluid viscosity, respectively. Both of them are functions of the time and space, implying that $\rho = \rho(\underline{x}, t)$ and $\mu = \mu(\underline{x}, t)$. The tensor $\underline{\underline{D}}$ shown above denotes the rate of deformation, with the components denoted by $D_{ij} = \frac{1}{2}(u_{i,j} + u_{j,i})$. In addition to the stress tensor given by $-p\underline{\underline{I}} + 2 \underline{\underline{D}}$, where $\underline{\underline{I}}$ is the identity matrix, the other source term capable of resulting in flow acceleration is the surface tension $\underline{\underline{T}}$ concentrated solely on the two-fluid interface, which is denoted by the phase field function Φ .

In this study, the surface tension will be modified as the body force and is applied at the interface. In other words, the surface tension per unit interfacial area is given by

$$\underline{\underline{T}} = \sigma \kappa \underline{\underline{n}} \quad (3)$$

In the above, σ is denoted as the surface tension coefficient, κ is the curvature of the interface and the unit outward normal vector $\underline{\underline{n}}$ along the interface is normally

pointed to the surrounding liquid. One can express the normal and curvature of an interface in terms of Φ as $\underline{n} = \nabla\Phi/|\nabla\Phi|$ and $\kappa = \nabla \cdot \nabla\Phi/|\nabla\Phi|$. This clearly explains why the Navier-Stokes equations need to be formulated within the framework of level set method. In this study, the curvature term is approximated by the second-order accurate central scheme.

The above equations cast in the dimensional form will be normalized for the sake of general application. Taking $u_r, \ell_r, t_r, \rho_r g_r \ell_r, \rho_r, \mu_r$ as the referenced values for the respective velocity, length, time, pressure, density and viscosity, the normalized (or dimensionless) continuity equation remains unchanged.

$$\begin{aligned} \frac{\partial \underline{u}}{\partial t} + (\underline{u} \cdot \nabla) \underline{u} = & \frac{1}{\rho} (-\nabla p + \frac{1}{Re} \nabla \cdot (2 \underline{D}) \\ & + \frac{1}{We} \underline{F}_s) + \frac{1}{Fr^2} \underline{e}_g \end{aligned} \quad (4)$$

where \underline{e}_g is the unit gravitational direction vector and the Reynolds number (Re) is given by $Re = \rho_r u_r \ell_r / \mu_r$. Another characteristic parameter We is known as the Weber number, which is defined as $\rho_r u_r^2 \ell_r / \sigma$ and $Fr = V_r / \sqrt{gL_r}$ is the Froude number. Both density and viscosity will be smoothly approximated by $\rho = \rho_1 + (\rho_2 - \rho_1)\Phi$ and $\mu = \mu_1 + (\mu_2 - \mu_1)\Phi$, where ρ_i and μ ($i=1, 2$) are the dimensionless densities and viscosities of the two investigated fluids, respectively.

Numerical model

In this paper, the advection term in the level set equation is discretized using the dispersion- relation-preserving (DRP) dual-compact scheme [22], and the advection term in the momentum equation is discretized using the multi-dimensional DRP upwinding scheme [23].

The underlying idea in the DRP method is as follows: to physically predict the first derivative term accurately, the dispersive nature embedded in it must be retained as much as possible. The reason for this is that the dispersion relation governs the relationship between the angular frequency and the wavenumber of the first-order dispersive term [24]. In other words, it is possible to predict the solution accurately provided that the dispersion relation is well preserved. To achieve this, we combine the Taylor series expansion analysis with the Fourier transform analysis to derive the discretized coefficients. For details of the derivations, the interested reader is invited to refer to [22] and [23].

I. Dispersion-relation-preserving scheme

Assume that the first derivative term $\partial\phi/\partial x$, in equation (4), and the second derivative term $\partial^2\phi/\partial x^2$ are approximated within the following three-point compact framework

$$a_1 \frac{\partial\phi}{\partial x}|_{i-1} + \frac{\partial\phi}{\partial x}|_i = \frac{1}{h} (c_1\phi_{i-1} + c_2\phi_i + c_3\phi_{i+1}) - h \left(b_1 \frac{\partial^2\phi}{\partial x^2}|_{i-1} + b_2 \frac{\partial^2\phi}{\partial x^2}|_i + b_3 \frac{\partial^2\phi}{\partial x^2}|_{i+1} \right) \quad (5)$$

$$\bar{b}_1 \frac{\partial^2\phi}{\partial x^2}|_{i-1} + \frac{\partial^2\phi}{\partial x^2}|_i + \bar{b}_3 \frac{\partial^2\phi}{\partial x^2}|_{i+1} = \frac{1}{h^2} (\bar{c}_1\phi_{i-1} + \bar{c}_2\phi_i + \bar{c}_3\phi_{i+1}) - \frac{1}{h} (\bar{a}_1 \frac{\partial\phi}{\partial x}|_{i-1} + \bar{a}_2 \frac{\partial\phi}{\partial x}|_i + \bar{a}_3 \frac{\partial\phi}{\partial x}|_{i+1}) \quad (6)$$

For terms $\partial\phi/\partial y$ and $\partial^2\phi/\partial y^2$, they can be similarly expressed along the y -direction. Note that the compact schemes for $\partial\phi/\partial x|_i$ and $\partial^2\phi/\partial x^2|_i$ are not independent of each other. They are rather strongly coupled through terms $\partial\phi/\partial x|_{i-1}$, $\partial\phi/\partial x|_i$, $\partial\phi/\partial x|_{i+1}$, $\partial^2\phi/\partial x^2|_{i-1}$, $\partial^2\phi/\partial x^2|_i$, $\partial^2\phi/\partial x^2|_{i+1}$, ϕ_{i-1} , ϕ_i and ϕ_{i+1} . For the sake of description, we consider the above equations only for the case involving the upwind (backward) case.

Approximation of $\partial^2\phi/\partial x^2$ can normally be accomplished by applying the central schemes because discretization error tends to be dissipative. The weighting coefficients shown in equation (6) are then determined solely according to the modified equation analysis to provide higher spatial accuracy. Derivation of the coefficients $\bar{a}_1 \sim \bar{a}_3$, \bar{b}_1 , \bar{b}_3 and $\bar{c}_1 \sim \bar{c}_3$ is as follows. We start by applying the Taylor series expansions for $\phi_{i\pm 1}$, $\partial\phi/\partial x|_{i\pm 1}$ and $\partial^2\phi/\partial x^2|_{i\pm 1}$ with respect to ϕ_i , $\partial\phi/\partial x|_i$ and $\partial^2\phi/\partial x^2|_i$. This is followed by elimination of the leading error terms derived in the modified equation. The coefficients then can be derived for Eq. (6) as $\bar{a}_1 = -9/8$, $\bar{a}_2 = 0$, $\bar{a}_3 = 9/8$, $\bar{b}_1 = 1/8$, $\bar{b}_3 = -1/8$, $\bar{c}_1 = 3$, $\bar{c}_2 = -6$, $\bar{c}_3 = 3$.

Dispersion-relation-preserving governs the relationship between angular frequency and the wavenumber of the first-order dispersive term [24]. The dispersive nature embedded in $\partial\phi/\partial x|_i$ can largely be retained if the first derivative term from equation (9) is modeled suitably. To preserve the dispersion relation, we applied the Fourier transform and its inverse for ϕ , as presented below:

$$\begin{aligned}\phi(\alpha) &= \frac{1}{2\pi} \int_{-\infty}^{+\infty} \phi(x) \exp(-i\alpha x) dx, \\ \phi(x) &= \int_{-\infty}^{+\infty} \phi(\alpha) \exp(i\alpha x) d\alpha\end{aligned}\quad (7)$$

Note that notation \mathbf{i} is equal to $\sqrt{-1}$. By performing a Fourier transform on each term shown in equations (6) and (7), the expressions of the actual wave number α for these two equations can be derived as

$$\begin{aligned}\mathbf{i}\alpha h (a_1 \exp(-i\alpha h) + 1) &\simeq c_1 \exp(-i\alpha h) + c_2 + c_3 \exp(i\alpha h) \\ &\quad - (\mathbf{i}\alpha h)^2 (b_1 \exp(-i\alpha h) + b_2 + b_3 \exp(i\alpha h)) \\ (\mathbf{i}\alpha h)^2 \left(-\frac{1}{8} \exp(-i\alpha h) + 1 - \frac{1}{8} \exp(i\alpha h)\right) &\simeq 3 \exp(-i\alpha h) \\ -6 + 3 \exp(i\alpha h) - \mathbf{i}\alpha h \left(-\frac{8}{9} \exp(-i\alpha h) + \frac{8}{9} \exp(i\alpha h)\right) &\quad (8)\end{aligned}$$

In an approximate sense, the effective wavenumbers α' , α'' have the same expressions as those shown on the right-hand sides of equation (8) [23]. Therefore, we can express α' and α'' as follows:

$$\begin{aligned}\mathbf{i}\alpha' h (a_1 \exp(-i\alpha h) + 1) &= c_1 \exp(-i\alpha h) + c_2 + c_3 \exp(i\alpha h) \\ &\quad - (\mathbf{i}\alpha'' h)^2 (b_1 \exp(-i\alpha h) + b_2 + b_3 \exp(i\alpha h)) \\ \mathbf{i}\alpha' h \left(-\frac{8}{9} \exp(-i\alpha h) + \frac{8}{9} \exp(i\alpha h)\right) &= 3 \exp(-i\alpha h) - 6 \\ + 3 \exp(i\alpha h) - (\mathbf{i}\alpha'' h)^2 \left(-\frac{1}{8} \exp(-i\alpha h) + 1 - \frac{1}{8} \exp(i\alpha h)\right) &\quad (9)\end{aligned}$$

After solving equation (9), α' and α'' can be derived as

$$\begin{aligned}\alpha' h &= -\mathbf{i}(24b_1 \exp(-2i\alpha h) + c_1 \exp(-2i\alpha h) + c_3 + c_1 + 24b_1 \\ &\quad + c_2 \exp(-i\alpha h) + 24b_2 \exp(-i\alpha h) + 24b_3 - 48b_1 \exp(-i\alpha h) \\ &\quad - 8c_1 \exp(-i\alpha h) - 48b_3 \exp(i\alpha h) + 24b_2 \exp(i\alpha h) \\ &\quad + 24b_3 \exp(2i\alpha h) - 48b_2 + c_2 \exp(i\alpha h) + c_3 \exp(2i\alpha h)) \\ \alpha'' h &= [-(3 \exp(-i\alpha h) - 6 + 3 \exp(i\alpha h) \\ &\quad - 8c_3 \exp(i\alpha h) - 8c_2) / (-8 + \exp(i\alpha h) - 8a_1 \exp(-i\alpha h) \\ &\quad + a_1 \exp(-2i\alpha h) - 9b_1 \exp(-2i\alpha h) - 9b_2 \exp(-i\alpha h) \\ &\quad + 9b_2 \exp(i\alpha h) + 9b_3 \exp(2i\alpha h) + a_1 + 9b_1 - 9b_3 + \exp(i\alpha h)) \\ &\quad - \mathbf{i}\alpha' h \left(\frac{8}{9} \exp(-i\alpha h) + \frac{8}{9} \exp(i\alpha h)\right) \\ &\quad / \left(-\frac{1}{8} \exp(-i\alpha h) + 1 - \frac{1}{8} \exp(i\alpha h)\right)]\end{aligned}\quad (10)$$

To enhance the dispersive accuracy of α' , it is required that $\text{Re}[\alpha' h] \approx \alpha h$, where $\Re[\alpha' h]$ denotes the real part of $\alpha' h$. This implies that $E(\alpha)$ as defined below should have a very small, and positive value. Define

$$\begin{aligned}
E(\alpha) &= \int_{-\frac{\pi}{2}}^{\frac{\pi}{2}} [W(\alpha h - \text{Re}[\alpha' h])]^2 d(\alpha h) \\
&= \int_{-\frac{\pi}{2}}^{\frac{\pi}{2}} [W(\gamma - \text{Re}[\gamma'])]^2 d\gamma
\end{aligned} \tag{11}$$

where $\gamma = \alpha h$, $\gamma' = \alpha' h$ and W is the weighting function which is selected to allow equation (11) to be analytically integrated. To make E the minimum, positive value, the following extreme condition is enforced

The solution of the above equation, in conjunction with the other six algebraic equations obtained using modified equations analysis, allows for the seven introduced unknowns (provided below) to be uniquely determined as $a=0.875$, $b_1=0.125$, $b_2=-0.249$, $b_3=0.00013$, $c_1=-1.936$, $c_2=1.997$, $c_3=-0.061$. It should be noted that the above upwinding scheme developed for $\partial\phi/\partial x$ can be shown to have spatial accuracy up to the fifth order from the following modified equations $\partial\phi/\partial x = \partial\phi/\partial x|_{\text{exact}} - 0.0007 h^5(\partial^6\phi/\partial x^6) + 0.0002 h^6(\partial^7\phi/\partial x^7) + 0.00005 h^7(\partial^8\phi/\partial x^8) + O(h^8) + \dots$. Please refer to [22] for details.

For the sake of completeness, we also present the dispersion and dissipation behavior for the present dual-compact scheme. The fundamental analysis begins with the definition of coefficients k_i and k_r for the dispersion and dissipation errors, respectively:

$$\begin{aligned}
k_i &= \text{Re}[\gamma'] \\
k_r &= \text{Im}[\gamma']
\end{aligned} \tag{12}$$

In the above, $\text{Re}[\gamma']$ denotes the real part of γ' ($\equiv \alpha' h$) and $\text{Im}[\gamma']$ denotes the imaginary part of γ' . In Figure 1(a) to (b), the predicted values of k_i and k_r are plotted against the modified wavenumber αh for the proposed dual-compact upwind scheme. Figure 1(a) illustrates that the proposed scheme is capable of providing excellent dispersion, which is crucial to the simulation of the phase field equation. The k_r value derived from the current upwind dual-compact scheme, does not precisely match the exact solution, due to the addition of artificial viscosity to enhance stability.

II. Semi-implicit Gear scheme and projection method

In our present study, the two phase flow equations are discretized by the Gear scheme as follows:

$$\begin{aligned}
\frac{3\underline{u}^{n+1,*} - 4\underline{u}^n + \underline{u}^{n-1}}{2\Delta t} &= -2[(\underline{u} \cdot \nabla)\underline{u}]^n + [(\underline{u} \cdot \nabla)\underline{u}]^{n-1} \\
+ 2\frac{1}{\rho^{n+1}}\left[\frac{1}{Re}\nabla \cdot (2\underline{D} - \nabla^2\underline{u})\right]^n \\
- \frac{1}{\rho^{n+1}}\left[\frac{1}{Re}\nabla \cdot (2\underline{D} - \nabla^2\underline{u})\right]^{n-1} \\
+ \left(\frac{1}{\rho}(-\nabla p + \frac{1}{Re}\nabla^2\underline{u} + \frac{1}{We}\underline{F}_s) + \frac{1}{Fr^2}\underline{e}_g\right)^{n+1,*} \quad (13)
\end{aligned}$$

Note that we compute $\nabla p^{n+1,*}$ using the second order backward difference:

$$\nabla p^{n+1,*} = 2\nabla p^n - \nabla p^{n-1} \quad (14)$$

Equation (14) may be expressed as a Helmholtz equation in the form $(\mathbf{I} + \mathbf{A})\underline{u}^{n+1} = \mathbf{F}$. There is no need for non-linear iteration for the present semi-implicit scheme. The intermediate velocity $\underline{u}^{n+1,*}$ is generally not divergence-free.

$$\frac{3(\underline{u}^{n+1} - \underline{u}^{n+1,*})}{2\Delta t} = -\frac{1}{\rho}\nabla p' \quad (15)$$

$$p^{n+1} = p^{n+1,*} + p' \quad (16)$$

Considering the divergence in equation (15), we can derive the Poisson equation for pressure correction as follows:

$$\nabla \cdot \left(\frac{1}{\rho}\nabla p'\right) = \frac{3(\nabla \cdot \underline{u}^{n+1,*})}{2\Delta t} \quad (17)$$

Solving equation (17), one can compute the corrected velocity $\underline{u}^{n+1} = \underline{u}^{n+1,*} - 2/3\Delta t(1/\rho\nabla p')$, and the pressure $p^{n+1} = p^{n+1,*} + p'$.

III. Velocity-pressure coupling

When solving the incompressible flow equation, special care must be taken for the velocity and pressure coupling. While a staggered grid has been demonstrated to be able to eliminate the odd-even decoupling problem, the resulting program complexity is still a key task. For our purposes, we use a semi-staggered grid to couple the velocity and pressure [27]. The velocity vectors are stored at the edge of the cell, whereas pressure and other scalar fields are stored at the center, as shown in Figure 2. The programming complexity is much lower for this grid system, compared to the staggered grid, and the coupling may be easily achieved if one employs a pressure interpolation from cell center to edge.

Numerical results

In this section, we present results for our solution. For the benchmark problems, we list the order of accuracy, the conservation of total mass, and the contours for the computed results. Finally, we compare our results with experimental and numerical results for three two-phase flow benchmark problems.

I. Dam-break problem

The first problem without considering surface tension simulates the sudden collapse of a rectangular column of water onto a planar surface. This classical problem, known as the dam break problem, has been frequently employed to validate the code for predicting free surface hydrodynamics. In addition to the hydraulic importance of this problem, both experimental [31] and numerical results [32] are available for making a direct comparison.

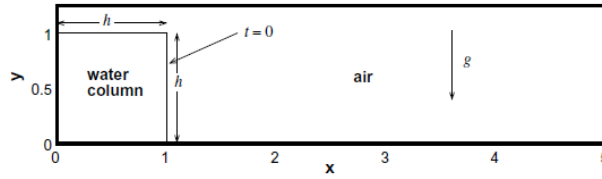


Fig. 1. Schematic of the initial water column for the dam break problem considered

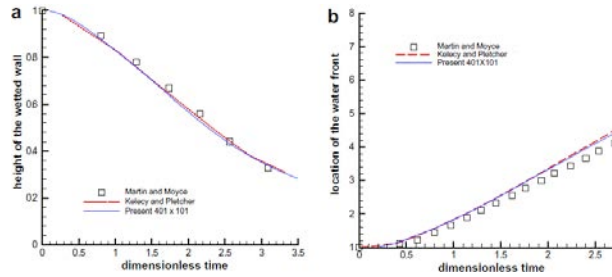


Fig. 2. Comparison of the predicted surge front location and the water column height with the experimental data and the numerical results of Kelecly and Pletcher.

(a) height of the wetted wall; (b) location of the water front.

In the current calculation, the fluid properties are considered to be the same as those given in [32]. The initially prescribed height of the water column schematic in Figure 1 is $h=1$. The results for the collapsed water will be predicted at $Re=42792$ in the domain containing 301×76 and 401×101 nodal points. The predicted heights

of the collapsed water column will be plotted against the dimensionless time defined in [32]. Good agreement with the experimental result given in [31] is clearly demonstrated in Figure 2 for the predicted surge front location and the water column height. The predicted time-evolving free surfaces in Figure 3 are compared also favorably with the finite element solution of Kelecy and Pletcher [32]. As Figure 4 shows for the ratio of the temporal water against the initial water column, the conservative property built in the modified level set method is still retained quite well.

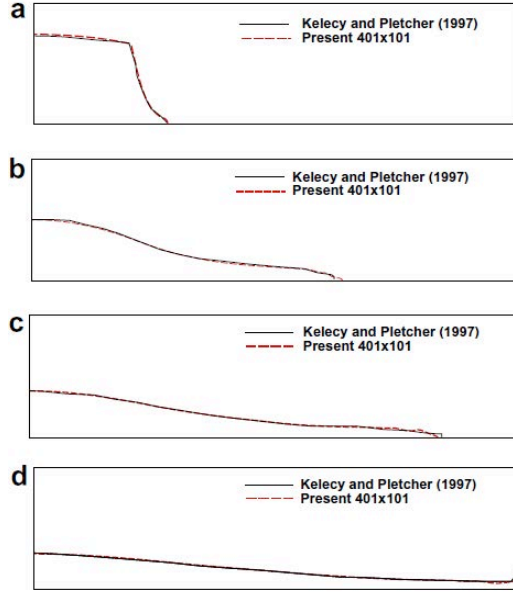


Fig. 3. Comparison of the predicted free surfaces, obtained at 401×101 grids, with those of Kelecy and Pletcher for the two-dimensional broken dam problem. (a) $t=0.6$; (b) $t=1.8$; (c) $t=2.4$; (d) $t=3.0$.

II. Bubble rising problem

We then investigate the time-evolving interface problem where surface tension needs to be taken into account. The problem under investigation considers the evolution of a stationary bubble, that is driven by surface tension, in a container partially filled with the viscous fluid of height $3.5D$ and width $3.0D$, where D is the initial diameter of the bubble. The main reason for modeling the gas bubble rising from rest in the incompressible fluid flow under buoyancy is due to a considerable amount of available experimental results in the literature [33,34].

Modelling of a rising bubble, schematic in Figure 5, needs to specify the ratios of physical properties for the gas and liquid. The fluid-gas density and viscosity ratios are specified respectively as $\rho_\ell/\rho_g=2.0$ and $\mu_\ell/\mu_g=2.0$. In addition, the problem

under investigation is characterized by another two dimensionless parameters, namely, $Re(D)^{3/2} \sqrt{g\rho_\ell/\mu_\ell}$ and $We = \rho_\ell g D^2 / \sigma$, where Re and We are denoted as the Reynolds and Weber numbers, respectively. The subscripts ℓ and g correspond to the fluid surrounding the bubble and the fluid inside the bubble, respectively. Initially, the bubble center is located stationary at $(1.5D, 1.5D)$ in the flow, which is at rest everywhere. The whole domain will be considered rather than simply specifying the axially symmetric condition to avoid a possible development of Conda effect. As is usual, no-slip conditions are specified along the horizontal and vertical walls.

As the former test problem, the bubble area is excellently preserved. We have also conducted the analysis with the physical density ratio of 1000, considered by Sussman et al. [19], to simulate the bubble rising problem. The predicted time-evolving free surfaces and bubble interfaces, obtained in 144×144 grids with $Re = 100$ and $We = 200$, are plotted in Figure 6.

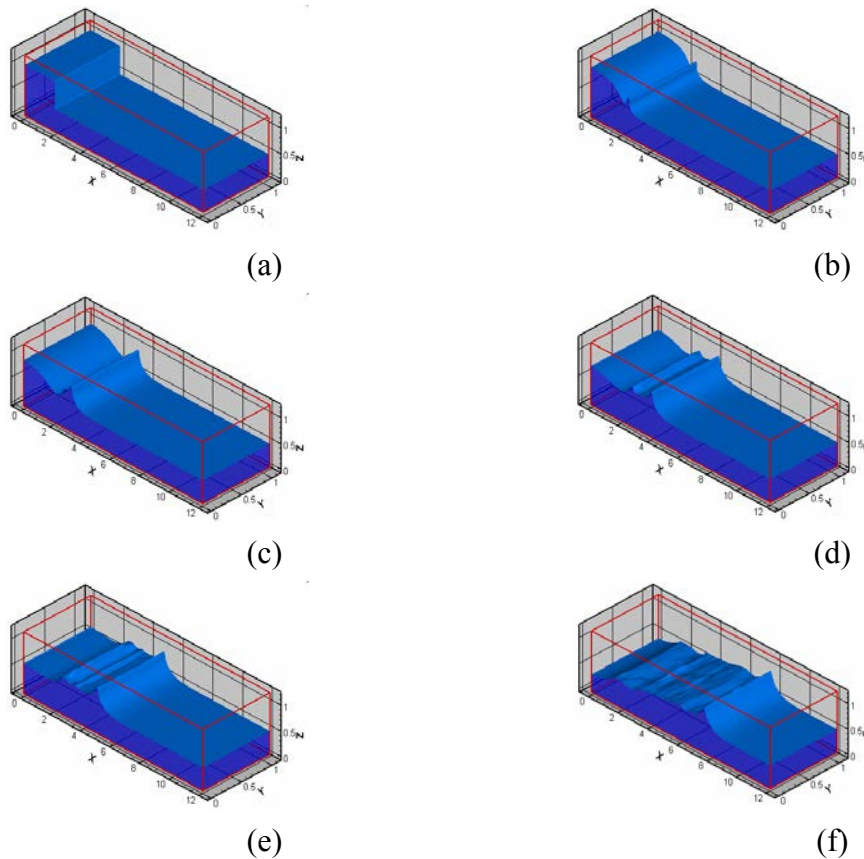


Fig. 4(a). Numerical simulation of dam-break wave surface change over time (downstream water depth is 0). (a) $t=0s$; (b) $t=1.0s$; (c) $t=2.0s$; (d) $t=3.0s$; (e) $t=4.0s$; (f) $t=7.0s$.

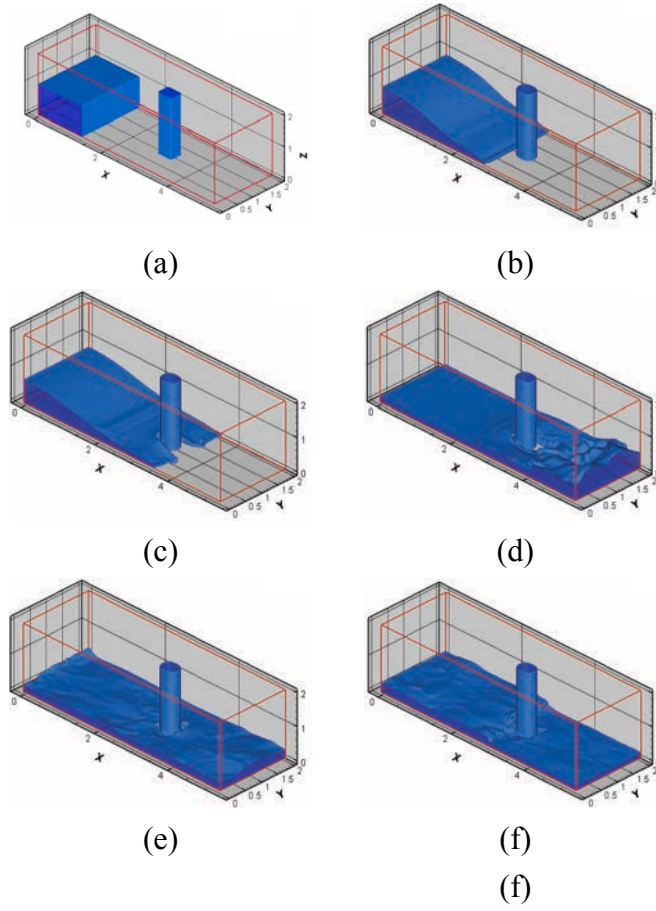


Fig. 4(b). Numerical simulation of the downstream side of the dam-break wave impulse column. (a) $t=0s$; (b) $t=1.5s$; (c) $t=2.0s$; (d) $t=7.0s$; (e) $t=14.0s$; (f) $t=20.0s$.

III. Water droplet falling problem

We also investigate a water droplet falling through the air and hitting the originally planar free surface. The dimensionless physical properties under current investigation are set to be the same as those given in Sussman et al. [36], namely, $\mu_1=1$, $\mu_2=0.0141$, $\rho_1=1$, $\rho_2=0.00123$. The drop is initially accelerated with a fictitious gravitational force $1/Fr^2 = 1/2$ for a total dimensionless time of 2. Afterwards, three dimensionless parameters for characterizing the flow motion are chosen as $Re=3518$, $Fr=1633$ and $We=220$, where the characteristic length and velocity are chosen as $10^{-3}m$ and $4 m/s$, respectively. All the calculations will be carried out at $\Delta x = \Delta y = 0.03125$ and $\Delta t = 5.0 \times 10^{-4}$ for the droplet with the dimensionless radius of 1.

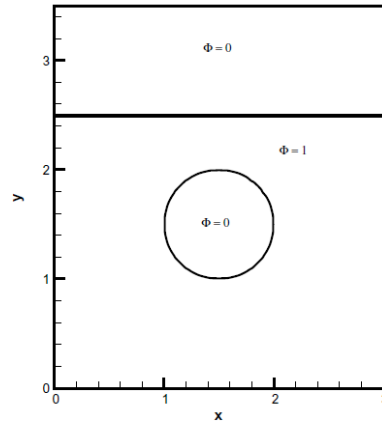


Fig. 5. Schematic of the initial condition for the bubble rising problem.

For the sake of enlightening the effect of surface tension, the case with consideration of surface tension is investigated for studying the interaction between the water droplet and the originally stationary water bounded by the free surface. The predimensionless dicted time-evolving droplet interface and free surface in Figure 21, plotted at the dimensionless times $t=0.0$, $t=2.4$ and $t=3.5$, are compared with those given in Sussman et al. [36]. As Figure 22 shows, the area-preserving feature remains also quite well for the case with consideration of surface tension.

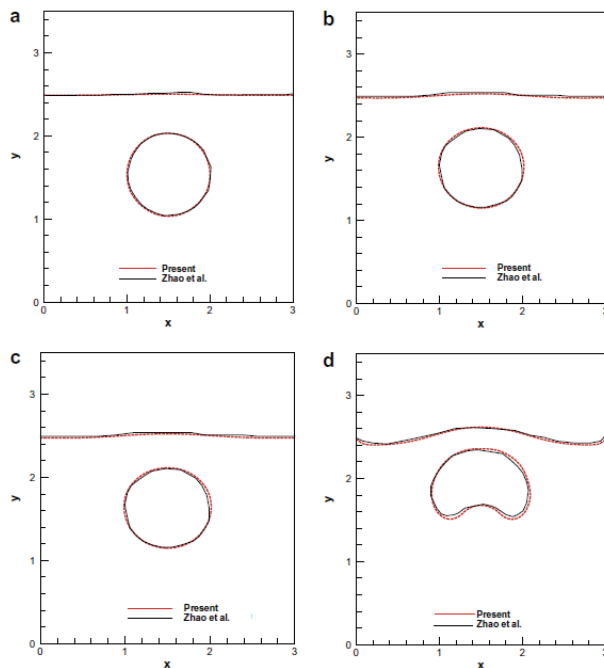
V. The actual terrain simulation

Finally, the study of the actual terrain of the development model in this paper. In the northern part of Taiwan freshwater Triple River area as an example, this section describes the geographic information system (GIS) and the actual DTM terrain apply in this mode, the final simulation results illustrate how GIS intususception were Application integration (reference Wu, 2005).

Numerical terrain model DTM data set covering the whole island, its mesh size of 40 square meters in Taiwan. Chelungpu fault along the Taipei area has a higher resolution of about 5 meters square grid of DTM data. Taiwan in 2006, Taiwan has completed DTM resolution of five meters square, since the information is not easy to build, general or special purposes higher resolution DTM data subject or purchase made by the applicant, DTM data system used in the present study through Feng Chia University (FCU) camp Infrastructure and Disaster Prevention Center achieved. The DTM data in accordance with the purpose or use of different methods of which have different sources of information, therefore, generally purchased in addition to the civil society, will also apply to land information system or purchase. Using ArcGIS software is based on the main shown in Figures 9-10.

Three simulated conditions assumed a sudden flood areas affected by the invasion, embankment or dike embankment overflow due to excessive upstream inflow, caused by a dike or notches to triple flooded areas. To penetrate the downstream boundary (outflow boundary), the basic depth of the river channel is set to 1.0 m, the number of simulated conditions set grid 108^2 , $\Delta x = \Delta y = 40\text{m}$. Then the numerical topographic data (DTM) construct a triple-area numerical model will want to simulate the terrain, DTM accuracy of $40\text{m} \times 40\text{m}$, is shown to simulate the actual terrain elevation schematic in Figure 11. Analog range is $4320 \times 4320\text{m}^2$ computational domain, including irregular terrain and meandering channels. The initial conditions for the simulation Manning $n=0.095$, $\text{CFL}=0.01$, simulation time from 0 seconds to 10,800 seconds.

Due to lack of information Tamsui triple section, under this part to Typhoon area in Taipei Bridge water line calendar for simulated conditions. Inflows to the two-dimensional variable Hager (1985) empirical formula proposed rewrite stream design flow line calendar to comply under the bridge in Taipei Typhoon area calendar water line, and then to the peak flow into the design flow line as the simulation calendar start. Where the bridge is located in the middle of the triple Taipei area, but is tentatively scheduled for inflow conditions, future data collection more complete good, if correct flow calendar line, after substituting the calculated results can show the triple area flooded condition.



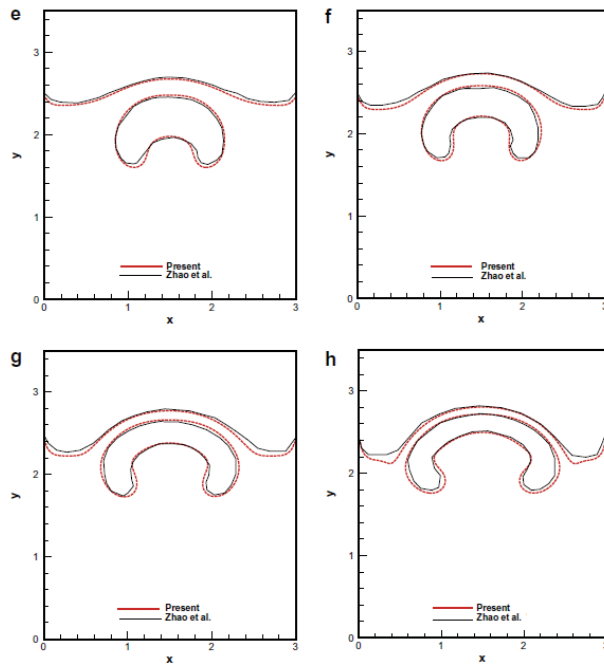
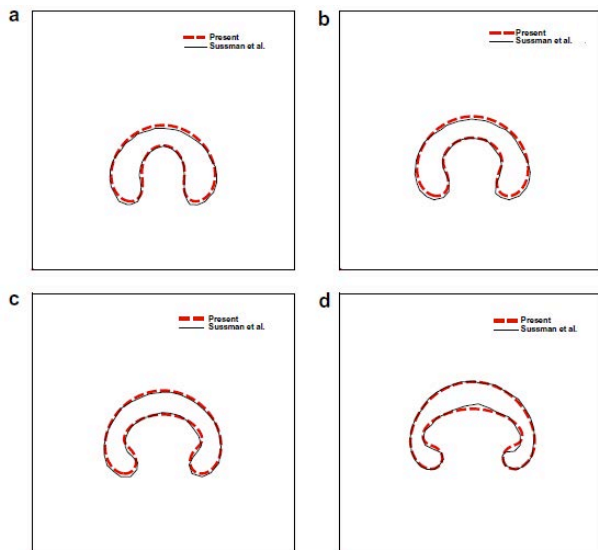


Fig. 6. Comparison of the predicted time-evolving free surfaces and bubble interfaces, obtained at 241×281 grids, with those of [35] for the case without considering surface tension. (a) $t=0.5$; (b) $t=1.0$; (c) $t=1.5$; (d) $t=2.0$ (e) $t=2.5$; (f) $t=3.0$; (g) $t=3.5$; (h) $t=4.0$.



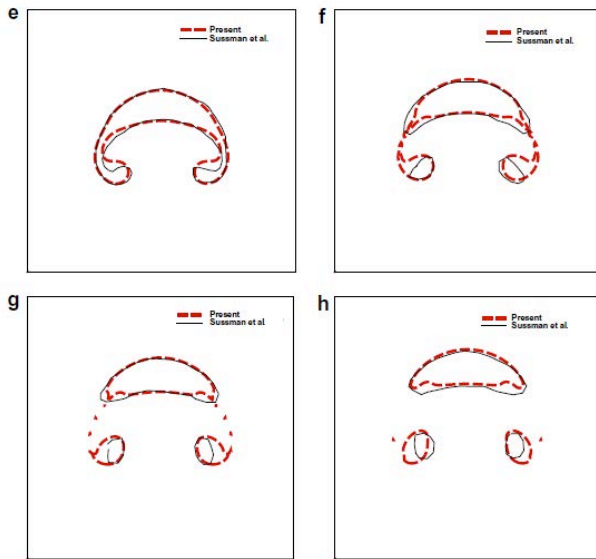


Fig. 7. Comparison of the predicted time-evolving free surfaces and bubble interfaces, obtained at 144×144 grids, with those of [19] for the case considering surface tension. (a) $t=2.8$; (b) $t=3.2$; (c) $t=3.6$; (d) $t=4.0$ (e) $t=4.4$; (f) $t=4.8$; (g) $t=5.2$; (h) $t=5.6$.

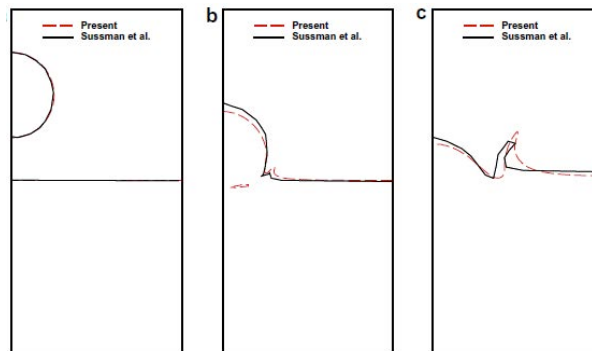


Fig. 8. Comparison of the predicted interfaces with those of Sussman et al. [36] for the droplet problem investigated in 257×257 grids. (a) $t=0.0$; (b) $t=2.4$; (c) $t=3.5$.

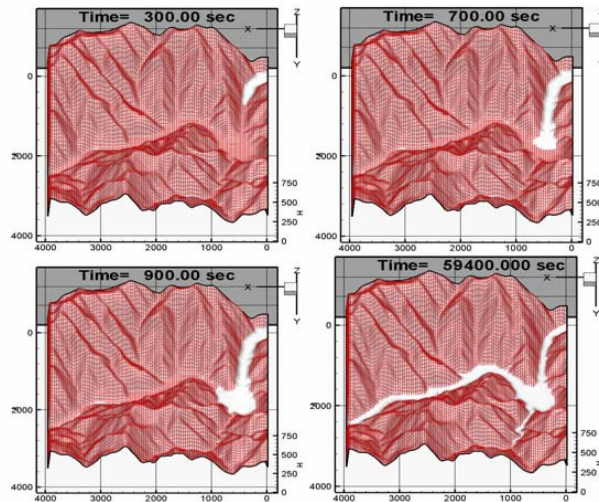


Fig. 9. Flooding flow simulation of the actual terrain conditions change (Reference Wu, 2005)

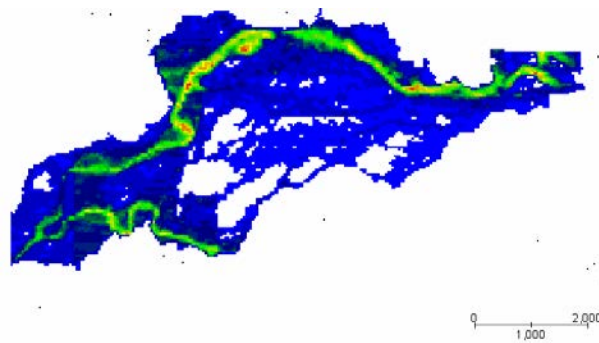


Fig. 10. Flooding potential analysis indicate (Wu, 2005)

Conclusion remarks

The differential equation employed to model the evolving interface should accommodate the conservative interface property. This underlying transport equation should also have the ability to compress the level set function and can, therefore, sharpen the interface. For the stabilization reason, an artificial viscosity that is sufficient to suppress the oscillations in the vicinity of interface, at which a fairly high gradient solution may be present, is explicitly added to the formulation. The derived conservative level set method will be split into the conventional level set method for the advection of the level set function and the other inhomogeneous equation, with the compressive flux and source terms being nonlinear with respect to the level set function, for compressing the interface profile. The finite volume advection scheme implemented in the advection step of the conservative level set

method should yield a predicted solution that is dispersively very accurate. Both of the proposed DRP advection scheme and compact pressure gradient scheme applied in non-staggered grids have been verified analytically.

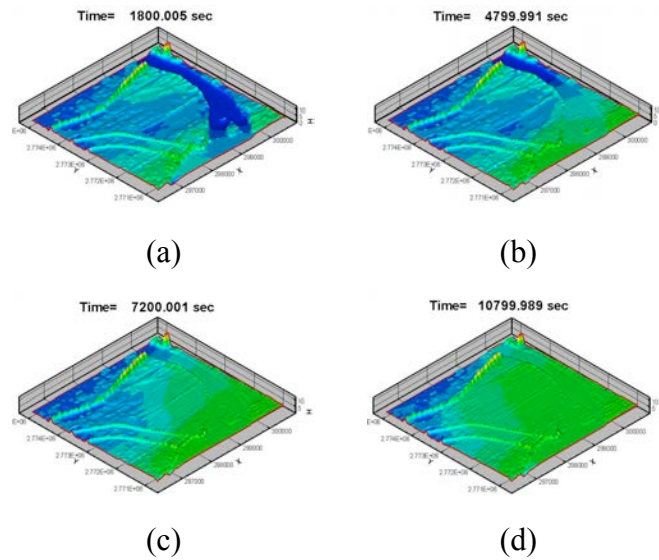


Fig. 11. Simulate the actual terrain level changes (a) $t=1800s$; (b) $t=4800s$; (c) $t=7200s$; (d) $t=10800$.

Acknowledgements

The financial supports provided by the Ministry of Science and Technology (MOST) under grants MOST 102-2221-E-229-001 and MOST102-2119-M-492-004 are gratefully acknowledged.

References

Cheng, L. T., P. Burchard, B. Merriman, and S. Osher (2001) Motion of curves construction on surface using a level set approach, *Journal of Computational Physics*, Vol. 175, pp. 604-644.

Enright, D., R. Fedkiw, J. Ferziger, and I. Mitchell (2002) A hybrid particle level set method for improved interface capturing, *Journal of Computational Physics*, Vol. 183, pp. 83-116.

Iafrazi, A., A. D. Mascio, and E. F. Campana (2001), A level set technique applied to unsteady free surface flows, *International Journal for Numerical Methods in Fluids*, Vol. 35, pp. 281-297.

Jiang, G.-S., and D. Peng (2000) Weighted ENO schemes for hamilton-jacobi equations, *SIAM Journal on Scientific Computing (SISC)*, Vol. 21(6), pp. 2126-2143.

Janosi, I. M., D. Jan, K. Gabor Szabo, and T. Tel (2004) Turbulent drag reduction in dam-break flows, *Experiments in Fluids*, 37, pp. 219-229.

Jiang, G. S. and C. W. Shu (1996) efficient implementation of weighted ENO schemes, *Journal of Computational Physics*, Vol. 126, pp. 202-228.

Jiang, G. S. and C. C. Wu (1999) A high-order WENO finite difference scheme for the equations of ideal magnetohydrodynamics, *Journal of Computational Physics*, Vol. 150, pp. 561-594.

Kelecy, F. J., and R. H. Pletcher (1997) Comparison of physical and numerical dam-break simulations, *Journal of Environmental Science and Engineering*, Vol. 22, pp. 429-443.

Lin, C. L., H. Lee, T. Lee, and J. Weber (2005) A level set characteristic Galerkin finite element method for free surface, *International Journal for Numerical Methods in Fluids*, Vol. 49, pp. 521-574.

Osher, S., and J. A. Sethian (1998) Fronts propagating with curvature dependent speed: algorithms based on Hamilton-Jacobi formulations, *Journal of Computational Physics*, Vol. 79, pp. 12-49.

Sussman, M., and E. G. Puckett (2000) A coupled level set and volume of fluid method for computing 3D and axisymmetric incompressible two-phase flow, *Journal of Computational Physics*, Vol. 162, pp. 301-337.

Stansby, P. K., A. Chegini, and T. C. D. Barnes (1998) The initial stages of dam-break flow, *Journal of Fluid Mechanics*, Vol. 374, pp. 407-427.

Shu, C. W., and S. Osher (1989) Efficient implementation of essentially non-oscillatory shock-capturing schemes, *Journal of Computational Physics*, Vol. 83, pp. 32-78.

Sussman, M., A. S. Almgren, J. B. Bell, P. Colella, L. H. Howell, and M. L. Welcome (1999) An adaptive level set approach for incompressible two-phase flows, *Journal of Computational Physics*, Vol. 148, pp. 81-124.

Sussman, M., and E. Fatemi (1999) An efficient, interface-preserving level set redistancing algorithm and its application to interfacial incompressible fluid flow, *SIAM Journal on Scientific Computing*, Vol. 20, pp. 1165-1191.

Yue, W., C. L. Lin, V. C. Patel (2003) Numerical simulation of unsteady multi-dimensional free surface motions by level set method, *International Journal for Numerical Methods in Fluids*, Vol. 42, pp. 852-884.

J.A. Sethian, *Level Set Methods and Fast Marching Method*, Cambridge University Press, Cambridge, 2003.

M. Sussman, P. Smereka, S. Osher, A level set approach for computing solution to incompressible two-phase flow, *J. Comput. Phys.* 114 (1994) 146-159.

A.K. Tornberg, B. Enhquist, A finite element based level set method for multiphase flow applications, *Comput. Visual. Sci.* 3 (2000) 93-101.

M. Sussman, E.G. Puckett, A coupled level set and volume-of-fluid method for computing 3D and axisymmetric incompressible two-phase flows, *J. Comput. Phys.* 162 (2000) 301-337.

D. Enright, R. Fedkiw, J. Ferziger, I. Mitchell, A hybrid particle level set method for improved interface capturing, *J. Comput. Phys.* 183 (2002) 83-116.

Christophe Bogry, Christophe Bailly, A family of low dispersive and low dissipative explicit schemes for flow and noise computations, *J. Comput. Phys.* 194 (2004) 194-214.

C.K.W. Tam, J.C. Webb, Dispersion-relation-preserving finite difference schemes for computational acoustics, *J. Comput. Phys.* 107 (1993) 262-281.

I.A. Abalakin, A.V. Alexandrov, V.G. Bobkov, T.K. Kozubskaya, High accuracy methods and software development in computational aeroacoustics, *J. Comput. Methods Sci. Eng.* 2 (2003) 1-14.

Ladyzhenskaya, *The Mathematical Theory of Viscous Incompressible Flow*, Gordon and Breach, New York, 1969.

P. Lin, A sequential regularization method for time-dependent incompressible Navier–Stokes equations, *SIAM J. Numer. Anal.* 34 (1997) 1051-1071.

Tony W.H. Sheu, R.K. Lin, An incompressible Navier-Stokes model implemented on non-staggered grids, *Numer. Heat Trans., B Fundam.* 44 (2003) 277-294.

J.E. Pilliod, E.G. Puckett, Second-order accurate volume-of-fluid algorithms for tracking material interface, *J. Comput. Phys.* 199 (2004) 465-502.

U. Ghia, K.N. Ghia, C.T. Shin, High-Re solutions for incompressible flow using the Navier-Stokes equations and a multigrid method, *J. Comput. Phys.* 48 (1982) 387-411.

J. Martin, W. Moyce, An experimental study of the collapse of liquid columns on a rigid horizontal plane, *Philos. Trans.* 244 (1952) 312-324.

F.J. Kelecy, R.H. Pletcher, The development of a free surface capturing approach for multidimensional free surface flows in closed containers, *J. Comput. Phys.* 138 (1997) 939-980.

J.G. Hnat, J.D. Buckmaster, Spherical cap bubbles and shirt formation, *Phys. Fluids* 19 (1976) 182-194.

D. Bhaga, M.E. Weber, Bubbles in viscous liquids: shapes, wakes, and velocities, *J. Fluid Mech.* 105 (1981) 61-85.

Y. Zhao, H.H. Tan, B. Zhang, A high-resolution characteristics-based implicit dual time-stepping VOF method for free surface flow simulation on unstructured grids, *J. Comput. Phys.* 183 (2002) 233-273.

M. Sussman, A.S. Almgren, J.B. Bell, P. Colella, L.H. Howell, M.L. Welcome, An adaptive level set approach for incompressible two-phase flows, *J. Comput. Phys.* 148 (1999) 81-124.

Contact email: rklin@mail.tcmt.edu.tw